

Mapping tidal currents at a shallow tidal channel junction using the fluvial acoustic tomography system

Cong Xiao¹, Kiyoshi Kawanishi¹, Ryohei Torigoe¹, and Mohamad Basel Al Sawaf¹

¹Hiroshima University

November 26, 2022

Abstract

For the first time, we monitored continuous 2D tidal currents at a shallow tidal junction using the fluvial acoustic tomography (FAT) system during a period of ~ 34.4 days. The horizontal distribution and spatiotemporal variation of the tidal velocities were efficiently estimated by the inverse analysis method, and the reconstructed velocity patterns agreed well with the recorded acoustic Doppler current profiler series data. Additionally, the high frequency observation interval (1-min) used provided us with the opportunity to detect the rapid processes of the transformation of tidal current patterns during flood tide at the junction. These results further demonstrate that FAT is a potent tool for continuously mapping variable 2D tidal currents at shallow tidal junctions. Furthermore, tidal harmonic analyses of the reconstructed tidal currents were performed to clarify the nonlinear spatial evolution processes of the variations in tidal energy, when tides propagated from the estuary to the tidal junction. The sub-tide species (,) caused significant fortnightly variations in the tidal range along the tidal branches. The variations in the tidal current were dominated by semidiurnal species (D2: , , ,), followed by diurnal species (D1: , ,) and quarter-diurnal species (D4: ,). The / amplitude ratios were higher during low river discharge periods, signifying that the nonlinear tidal distortion varies with river discharge. River-tide interactions strongly affected tidal asymmetry. It is believed that this study provides further understanding of hydrological research in shallow tidal systems.

1 **Mapping tidal currents at a shallow tidal channel junction using the**
2 **fluvial acoustic tomography system**

3 **C. Xiao¹, K. Kawanisi^{1*}, R. Torigoe¹, M. B. Al Sawaf¹**

4

5 ¹ Department of Civil and Environmental Engineering, Graduate school of
6 Engineering, Hiroshima University, Higashihiroshima, Japan

7 *Corresponding author.

8 E-mail address: kiyosi@hiroshima-u.ac.jp (K. Kawanisi)

9

10 Key points:

- 11 ● Continuous 2D tidal currents were reconstructed by inverse method using 14
12 acoustic paths with six fluvial acoustic tomography (FAT) systems
- 13 ● 2D tidal currents inversed by FAT with short intervals during a period of ~34.4
14 days at a shallow tidal junction
- 15 ● Nonstationary river-tide dynamics at a shallow tidal junction were discussed based
16 on the inversed tidal currents

17

18 **Abstract**

19 For the first time, we monitored continuous 2D tidal currents at a shallow tidal
 20 junction using the fluvial acoustic tomography (FAT) system during a period of ~ 34.4
 21 days. The horizontal distribution and spatiotemporal variation of the tidal velocities
 22 were efficiently estimated by the inverse analysis method, and the reconstructed
 23 velocity patterns agreed well with the recorded acoustic Doppler current profiler series
 24 data. Additionally, the high frequency observation interval (1-min) used provided us
 25 with the opportunity to detect the rapid processes of the transformation of tidal current
 26 patterns during flood tide at the junction. These results further demonstrate that FAT is
 27 a potent tool for continuously mapping variable 2D tidal currents at shallow tidal
 28 junctions. Furthermore, tidal harmonic analyses of the reconstructed tidal currents
 29 were performed to clarify the nonlinear spatial evolution processes of the variations in
 30 tidal energy, when tides propagated from the estuary to the tidal junction. The sub-tide
 31 species (M_m , MS_f) caused significant fortnightly variations in the tidal range along the
 32 tidal branches. The variations in the tidal current were dominated by semidiurnal
 33 species (D2: M_2 , S_2 , N_2 , L_2), followed by diurnal species (D1: K_1 , O_1 , Q_1) and
 34 quarter-diurnal species (D4: M_4 , MS_4). The M_4/M_2 amplitude ratios were higher during
 35 low river discharge periods, signifying that the nonlinear M_4 tidal distortion varies with
 36 river discharge. River-tide interactions strongly affected tidal asymmetry. It is believed
 37 that this study provides further understanding of hydrological research in shallow tidal
 38 systems.

39 **1. Introduction**

40 Ocean acoustic tomography (OAT) was suggested as a potent oceanographic
 41 technique to investigate mesoscale oceanic phenomena (Munk et al., 1995).
 42 Furthermore, to extend the applications of OAT in coastal areas for the continuous
 43 monitoring of tidal currents, coastal acoustic tomography (CAT) was designed since
 44 the 1990s (Kaneko et al., 1994; Yamaguchi et al., 2005; Yamoaka et al., 2002). The
 45 fluvial acoustic tomography (FAT) system is a promoted generation can be utilized in
 46 quite shallow waters to investigate shallow currents, in riverine and tidal environments
 47 ranging from ~0.5 m up to 10 m depth (Kawanisi et al., 2010).

48 Some studies have already presented some applications using only two crossing
 49 paths to reconstruct velocity magnitude and direction; for example, the dam flush in a
 50 mountainous river was observed (Kawanisi et al., 2013) and the tidal flow in a shallow
 51 tidal channel was measured (Razaz et al., 2013). Furthermore, (Razaz et al. (2015);
 52 2016) positioned eight FATs in a shallow mountainous river and tidal channel to map
 53 depth-averaged current distributions. In the case of a mountainous river, although the
 54 boundary is meandering, there are no saltwater-wedge intrusion effects on sound
 55 propagation patterns. In the case of a tidal channel, salt-wedge intrusion effects occur

56 and should be carefully considered. A continuous measurement of 2D tidal current
57 fields at a shallow tidal junction with FAT to consider boundary and saltwater intrusion
58 effects has not been conducted. A previous study (Danial et al., 2019) at a tidal junction
59 using FAT only utilized two crossing paths to discuss tidal discharge and phase
60 difference.

61 The exploration of river-tide dynamics at tidal junctions, associated with the
62 interactions between river flow, tidal waves, and the bathymetry/geometrical shape of
63 tidal branches, have been scarcely studied (Danial et al., 2019). In tidally influenced
64 rivers, the intrusion of tides onto tidal junctions significantly complicates the processes
65 of flow division (Sassi et al., 2012). Dinehart and Burau (2005) observed current
66 variations at the tidal junction of the Sacramento River, which exhibited highly
67 asymmetrical patterns during ebb and flood. In tidally influenced estuaries, tidal
68 asymmetry and tide-induced residual circulations could generate a significant
69 influence on the distribution of currents over distributary channel networks.
70 Additionally, tidal propagation is strongly affected by river discharge in tidally
71 influenced rivers and vice versa (Lu et al., 2015). Owing to the effects of bottom
72 friction and river discharge, tidal waves propagating from the river mouth to upstream
73 areas become distorted and damped (Sassi & Hoitink, 2013). Previous studies only
74 focused on the results of subtidal water level structures for streamflow regimes in tidal
75 rivers, and most of the studies were based on numerical models (Cai et al., 2018; Guo et
76 al., 2014) or short/long time-series data, such as river discharges and water levels
77 recorded at several gauging stations (Guo et al., 2015). To the best of our knowledge,
78 detailed investigations on river-tide dynamics based on continuous 2D tidal current
79 data inversed by FAT have never been conducted.

80 In this study, we performed an experiment over one month with six FAT systems
81 at a shallow tidal junction, Hiroshima, Japan, in 2020. This study aims to characterize
82 the tidal regime in terms of a continuous 2D tidal current field, tidal asymmetry, tidal
83 dampening, the evolution of tidal constituents, and the propagation of tides at the
84 shallow tidal junction using FAT inversed results. We intend to collect several pieces of
85 evidence to demonstrate the response process of river-tide dynamics at the tidal
86 junction. The rest of this paper is structured as follows. Introductions of the study area
87 and methods are prepared in Section 2. Section 3 presents the inverse results at the
88 junction. Section 4 further discusses the tidal regime and river-tide interactions at the
89 junction based on the tidal currents reconstructed by the FAT. Finally, Section 5
90 presents the main conclusions in this study.

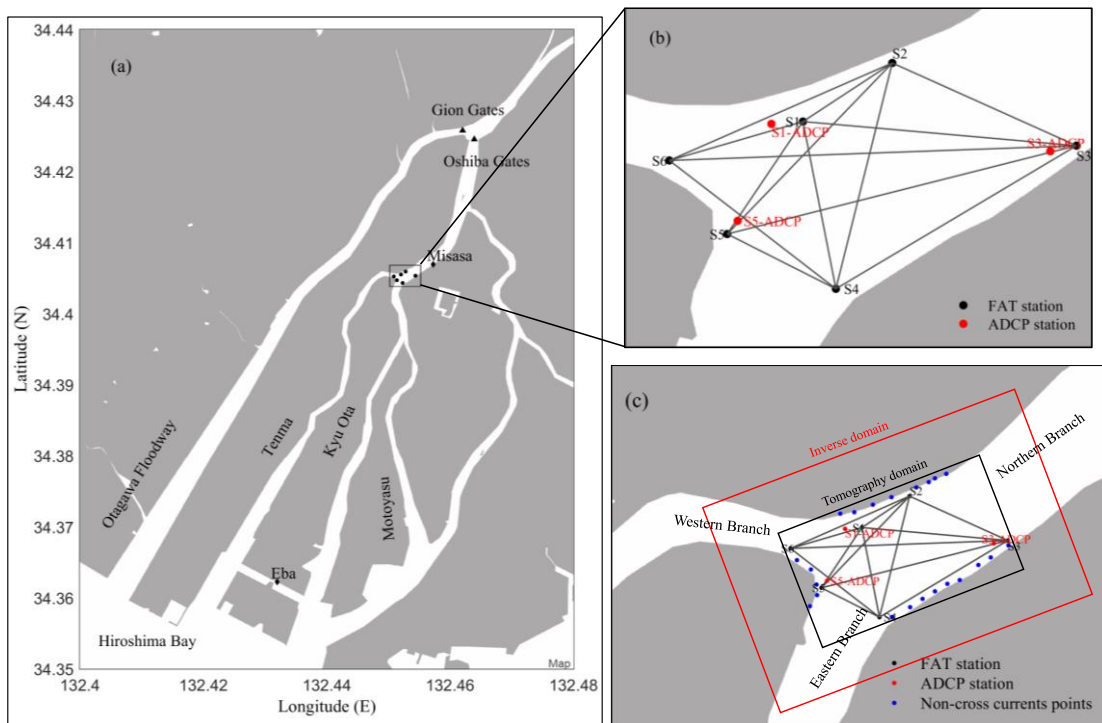
91 **2. Study area and methods**

92 **2.1 Study area**

93 The Ota River system is a network with several tide-dominated channels that
94 flows through Hiroshima City, west of Japan. As shown in Figure 1a, the Ota River

95 bifurcates around 9 km upstream from the river mouth into two major branches. The
 96 runoff in the Otagawa floodway are controlled by rows of Gion sluice gates, whereas
 97 the Oshiba sluice gates are always open throughout the year (Figure 1a). In this work,
 98 the studied tidal junction is situated in the mid-reach of the Ota River network, almost
 99 2.5 km downstream from the Oshiba gates and almost 5.8 km upstream from the river
 100 mouth, which is under the influence of saltwater intrusion and the freshwater discharge
 101 flowing from upriver areas. Salt-wedge intrusion in the Ota River can reach areas up to
 102 11.5 km upstream from the river mouth (Danial et al., 2019).

103 The shallow tidal junction involves three branches (Figure 1c): i) upstream (Kyu
 104 Ota River) is the northern branch, ii) downstream (Kyu Ota River) is the eastern branch,
 105 and iii) the Tenma River is the western branch. Danial et al. (2019) reported that the
 106 downstream (Kyu Ota River) is deeper and wider than the Tenma River. Riverbed
 107 levels for the eastern and western branches were approximately -3 T.P. m and -2 T.P. m,
 108 respectively. The northern branch is wider than both the eastern and western branches,
 109 and the riverbed level varies from -2.5 T.P. m to -3.0 T.P. m. In general, due to the
 110 frequent intrusion of saline water, freshwater discharge, and irregular bathymetry
 111 (Danial et al., 2019), the surveyed area is characterized by unsteady and complex flow
 112 distributions.

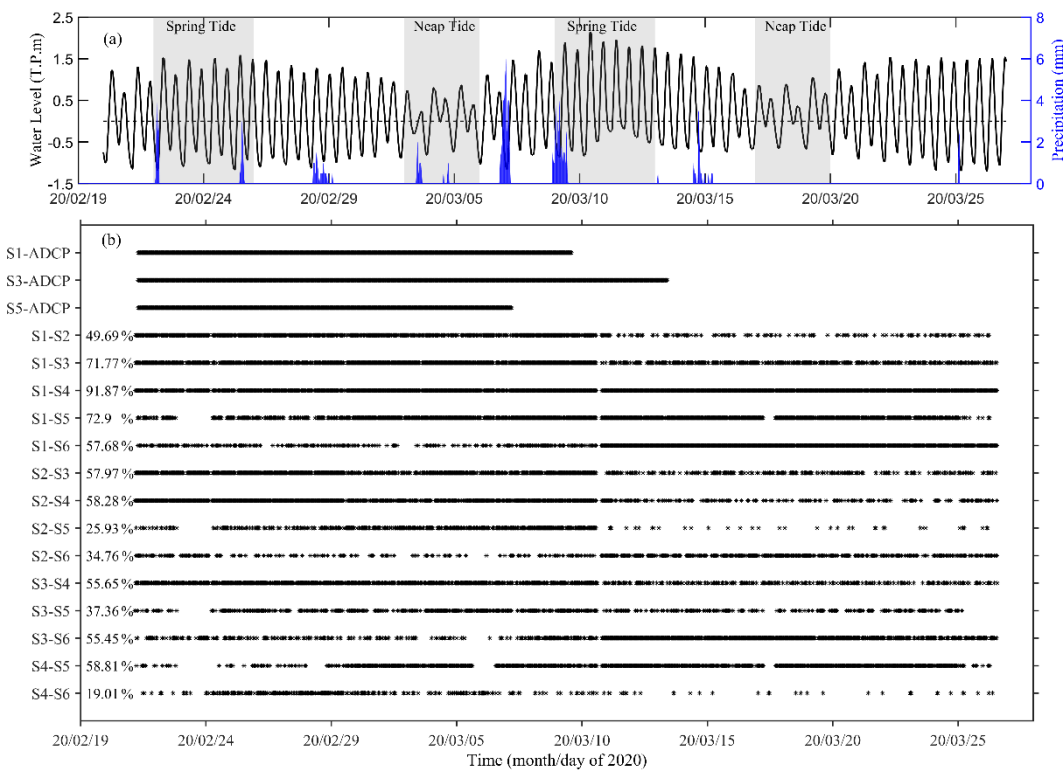


113
 114 Figure 1. Diagrams for the experimental area: The locations of the FAT stations (S1 to
 115 S6) and fixed ADCP stations are showed by black and red dots, respectively. Acoustica
 116 paths among the FAT stations are denoted by solid black lines.

117 2.2 Instruments and Methods

118 The FAT observation was carried out for ~ 34.4 days (February 21– March 26,
 119 2020), which covered two fortnightly tidal cycles (spring/neap cycle). As shown in

120 Figure 1b, six acoustic FAT transducers were placed along the riverbanks in an area
 121 almost 310 m length and 170 m width (Figure 1c). Simultaneous reciprocal
 122 transmissions were conducted along 14 transmission lines. During the observation
 123 period, acoustic signals with a 30-kHz central frequency were transmitted
 124 simultaneously from each source and then received by the other stations every minute.
 125 The transmitted sound was modulated by a M-sequence with the 9th order, increasing
 126 the processing gain by approximately 27.1 dB. The successful percentages of sound
 127 transmission data along 14 rays varied from 19% to 92% (Figure 2b). Missing data
 128 during the observation period were mainly triggered by the irregular, shallow region.
 129 Owing to the multiple reflections from the water surface and riverbed, the rays could
 130 not arrive at the receivers because of large transmission losses. The travel time
 131 difference series data were smoothed by a 1-h low-pass filter approach to erase the
 132 effects of the high-frequency noise, and, subsequently, be utilized in the inverse
 133 problem to estimate the 2D tidal current fields. The root mean squares error (RMSE)
 134 between the 1-min original and 1-h low-pass filtered travel time difference data
 135 fluctuated between 0.01 and 0.1 ms for the entire recorded data. The RMSE values
 136 caused errors in velocity that ranged from 0.06 to 0.21 m/s for all the station pairs, with
 137 a determined sound speed of 1475 m/s and constant station-to-station lengths.



138
 139 Figure 2. Synchronized FAT and ADCP measurements: (a) water level data was
 140 monitored at the Misasa gauging station, and precipitation data were acquired from the
 141 Japan Meteorological Agency, (b) observation periods of the fixed ADCP and time
 142 schedules of the successful percentages of reciprocal sound transmission between each
 143 settled station pair.

144

145 As shown in Figure 1b, three 2 MHz ADCPs (Aquadopp Profiler, Nortek) were
 146 placed to observe the 3D velocity variations in the water column, with a 60-second
 147 average interval and a 2-min sampling interval close to stations S1 and S3, and a 5-min
 148 sampling interval close to station S5. The bin size and blank distance were both set to
 149 0.1 m. The bin number was 50. Owing to the difference in battery life and the capacity
 150 of each ADCP, observations close to stations S1, S3, and S5 were performed from
 151 February 21 to March 9, February 21 to March 13, and February 21 to March 7,
 152 respectively. Along with the FAT measurements, several routes of Teledyne RDI
 153 StreamPro ADCP were performed along four transects (S1-S3, S1-S6, S3-S5, S4-S5)
 154 to provide reference velocity data on March 6, 2020. All data were referenced to
 155 bottom tracking. Each transect started from and stopped near the riverbank.

156 Because FAT primarily observes the sound travel time between the settled
 157 acoustic stations. Relying on the travel time differences of the acoustical station pairs,
 158 the horizontal distributions of the depth-averaged velocity can be effectively mapped
 159 by the inverse analysis. The inverse method has been employed by different
 160 researchers (Razaz et al., 2015; Yamaguchi et al., 2005; Yamoaka et al., 2002; Zhang et
 161 al., 2017; Zhu et al., 2015). In this work, we followed the basic formulas described in
 162 their papers.

163 Here, we only briefly introduce the method. Basically, the inverse method
 164 introduces a stream function to reconstruct the 2D depth-averaged current field within
 165 the tomography area. Consequently, the inverse issue resolves the unknown stream
 166 function based on the observation data recorded by FAT, and random errors are
 167 included in it. Thus, the inverse problem can be expressed in matrix notation as

$$y = Ex + e \quad (1)$$

168 Here, matrix y indicates the travel time difference for the actual station pairs, matrix E
 169 is the transform matrix that mainly rest with the FAT positions in the tomography area,
 170 x represents the unknown solution vectors for the Fourier expansion of the stream
 171 function, and e is the random error vector, corresponding to the observation and inverse
 172 method errors.

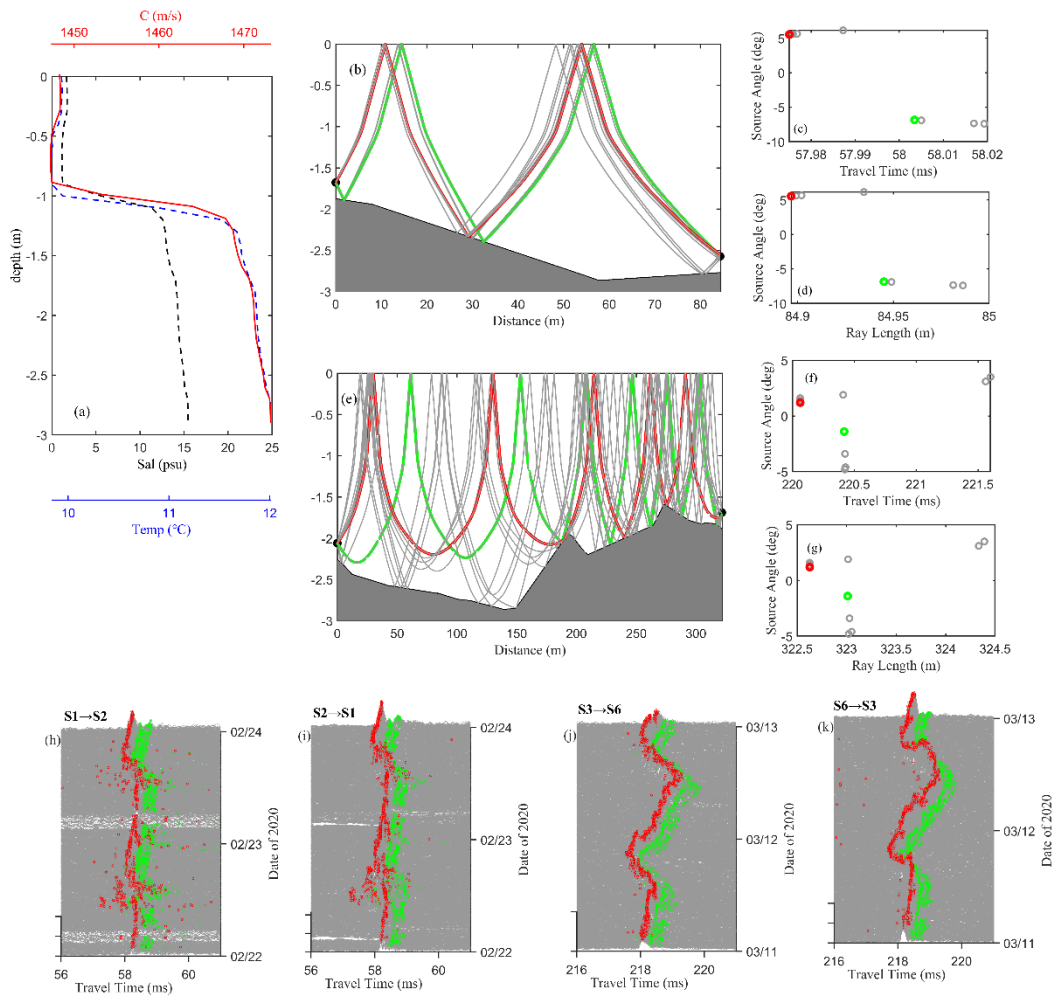
173 In order to decrease the periodicity effect in the solution, the inversion area should
 174 be adopted larger than the tomography area (Park & Kaneko, 2001). In this study, the
 175 inversion domain was set to 620 m length by 340 m width (Figure 1c). The number of
 176 truncated Fourier series coefficients was set to 3 in this study.

177 To consider the riverbank condition in the inverse problem, a set of linear
 178 equations $0 = \mathbf{u}(x_b, y_b) \cdot \mathbf{m}(x_b, y_b)$ were established, where \mathbf{m} represents the unit vector
 179 perpendicular to the riverbank at each given position (x_b, y_b) . Then, the linear equations
 180 were rewritten by the stream function, and these equations were added to the rows of
 181 Equation 1. Here, the riverbank condition was given at 22 points distributed over each
 182 riverbank, as seen in Figure 1c. Equation 1 is solved by the damped least-squares
 183 method clarified by Yamoaka et al. (2002) and Yamaguchi et al. (2005).

185 **3. Results**

186 **3.1 Typical ray simulation results**

187 Figure 3 demonstrates the ray patterns attained between the shortest station pairs
 188 (S1-S2, ~ 85 m) and the longest station pairs (S3-S6, ~ 322 m) by the ray-tracing
 189 method. Figure 3a demonstrates the typical vertical profiles of salinity, temperature,
 190 and sound speed documented by CTD at the upstream Misasa Bridge at high water.
 191 Owing to saltwater intrusion, deeper water had a higher salinity and temperature. The
 192 sound speed remained fairly constant at the upper levels, while at deeper levels, the
 193 sound speed showed a greater range, varying from 1450 to 1475 m/s.



194
 195 Figure 3. (a) Typical water temperature vertical profile, salinity vertical profile, and
 196 calculated sound speed vertical profile. (b)–(d) and (e)–(g) display the results of ray
 197 tracing along the shortest and longest transmission lines S1-S2 and S3-S6. (h), (i), (j),
 198 and (k) are elected stack graphs of the received correlation shapes drawn with the time
 199 axis (ms) along the shortest and longest transmission lines S1-S2 and S3-S6.

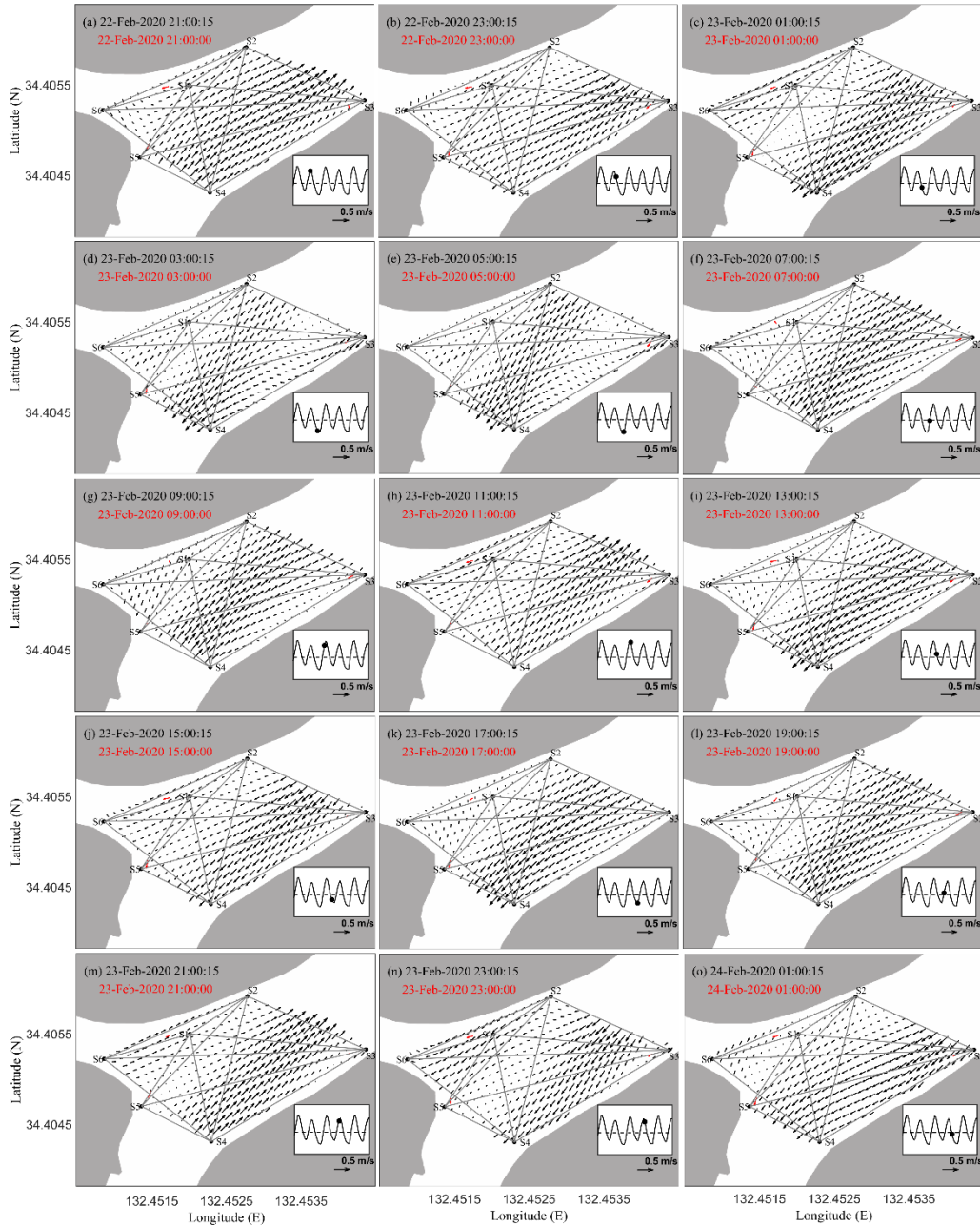
200
 201 Rays with large launch angles make multiple bottom and surface reflections; for

example, surface-bottom reflected rays with large angles caused the number of reflections to be more than 7 for the longest line S3-S6, and did often not arrive at the receiver because of the large transmission losses. Only the rays launched with small angles were successfully traced to simulate the sound traveling processes. The simulated values were roughly similar to the observed results. The rays launched with a positive angle that were linked to the first/largest arrival peak with a few surface-bottom reflections are marked with red lines (Figures 3b and 3e). Thus, the first peak points were selected as input data in the inverse analysis in this study (Figure 3).

3.2 Inverse results

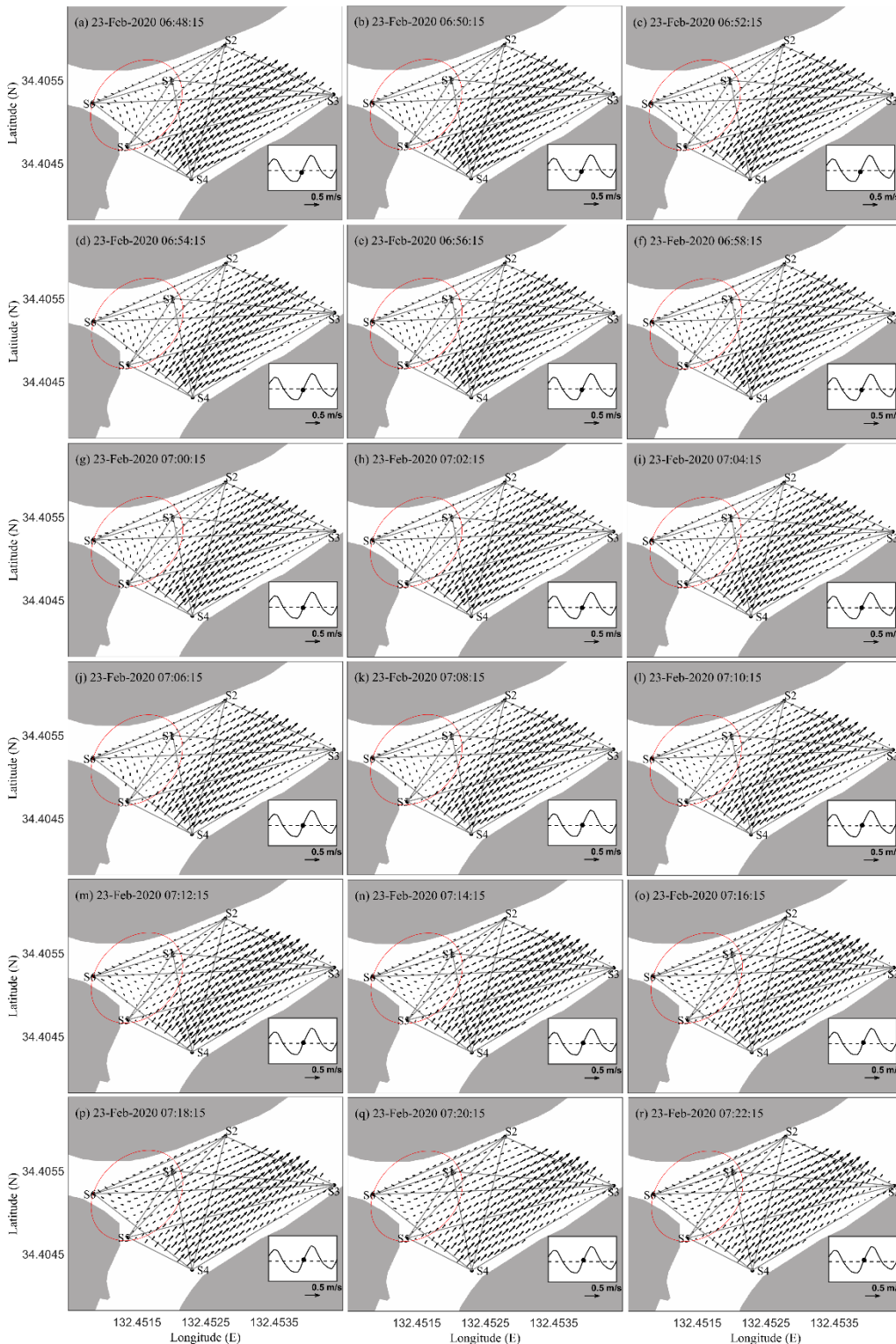
3.2.1 Depth-averaged tidal current distributions

The behaviors of the 2-hour interval 2D depth-averaged tidal currents (Figure 4) were reconstructed applying the inverse approach from 22 February to 24 February. The flow distribution pattern varied well with the tide, and the inversed velocity directions and magnitudes exhibited well agreement with those measured by the fixed ADCP near stations S1, S3, and S5. The temporal-spatial distributions of the tidal currents appeared realistic, considering the bathymetry and shape of the surveyed area (Figure 1). The currents tended to be slow and divided into two parts in the area around the confluence location (S5). During flood tide, significant landward currents flowed with a maximum speed value of 0.35 m/s; and during ebb tide, significant seaward currents were observed, with a maximum speed of 0.45 m/s. Temporally, the current distribution at the tidal junction showed that tidal currents during ebb tide were higher than during flood tide. Spatially, the behaviors of velocity distribution at the tidal junction indicated that tidal currents in the Kyu Ota River (eastern) region are stronger than those in the Tenma River (western) region. The flow directions in the study area can be explicated by the geometry of the junction, which leads to a large curvature in the current directions when flowing into the physical domain. Generally, as shown in Figure 4, streamlines within the tomography area tended to obey the curvature of the riverbanks.



230

231 Figure 4. Depth-averaged current distributions from 22 February to 24 February, 2020,
 232 at a 2-hour interval. The black and red arrows represent the velocities acquired by FAT
 233 and ADCP, respectively. The FAT stations are marked by black dots, and the actual
 234 acoustic transmission rays among the FAT stations are connected by the solid lines. The
 235 tidal phase of each sub-figure is signaled by a black dot on the water level at the lower
 236 right corner.
 237



238

239 Figure 5. Depth-averaged current distributions at 2-min intervals during flood tide. The
 240 FAT stations are marked by black dots, and the actual acoustic transmission rays among
 241 the FAT stations are connected by the solid lines. The tidal phase of each sub-figure is
 242 signaled by a black dot on the water level at the lower right corner.

243

In this study, the high frequency observation interval (1-min) provided the opportunity to explore the detailed processes of the formation of tidal current structures at the junction. In Figure 5, 2-min interval snapshots are presented during the flood tide around the higher tidal velocity. During the early flood tide period, significant landward currents flowed into the Kyu Ota River region. Meanwhile, the flow patterns marked within the red ellipse were weak compared with those in the Kyu Ota River region and flowed seaward (Figure 5a-5k). During the later flood tide period, the current patterns marked within the red ellipse were close to the velocities in the Kyu Ota River region and flowed landward (Figure 5l-5r). As shown in Figure 5, from Figure 5k to Figure 5p within the red ellipse, it took almost 12 min to complete the transformation of flow patterns. The dynamics of the flow patterns will be discussed later in this paper.

3.2.2 Comparison of FAT and ADCP results

Further, to verify the performance of the tomographic results, we compared the inverse estimates with the fixed ADCP data. As shown in Figure 6, the magnitudes and directions of the velocities reconstructed by FAT were agreement with to the fixed ADCP velocities (Figure 6). The RMSE values at S1, S3, and S5-ADCP were from 0.08 to 0.17 m/s and 0.05 to 0.17 m/s for the eastward and northward components, respectively. The coefficients of determination (R^2) of both components at S1, S3, and S5-ADCP were from 0.61 to 0.67 and 0.55 to 0.67, respectively. The large RMSE values related to S3-ADCP show an underestimation of the eastward components, which may result from the reason that the fixed ADCP monitors much smaller spatial scales of velocities. The ADCP sites did not overlap with any of the computational grid nodes, the generated velocities are the averaged values from the nearby points within the computational area that surrounded each fixed ADCP.

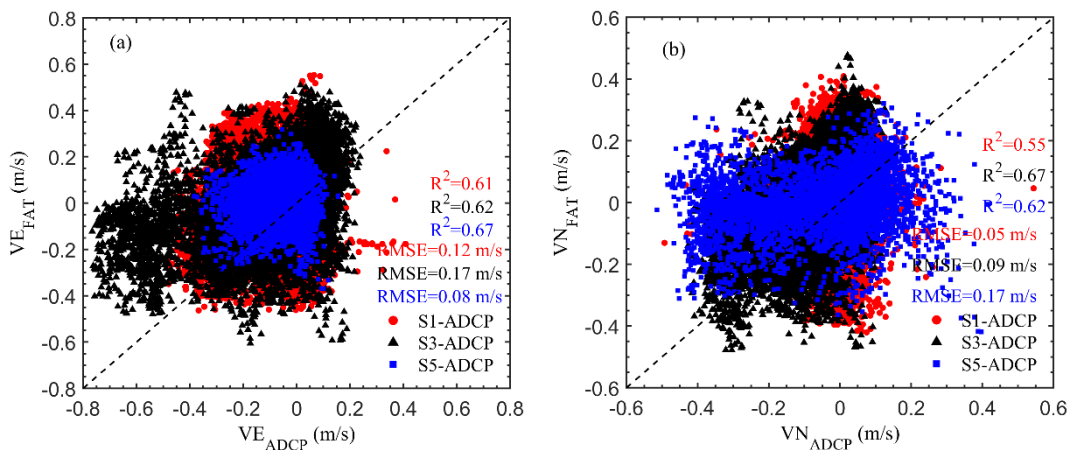
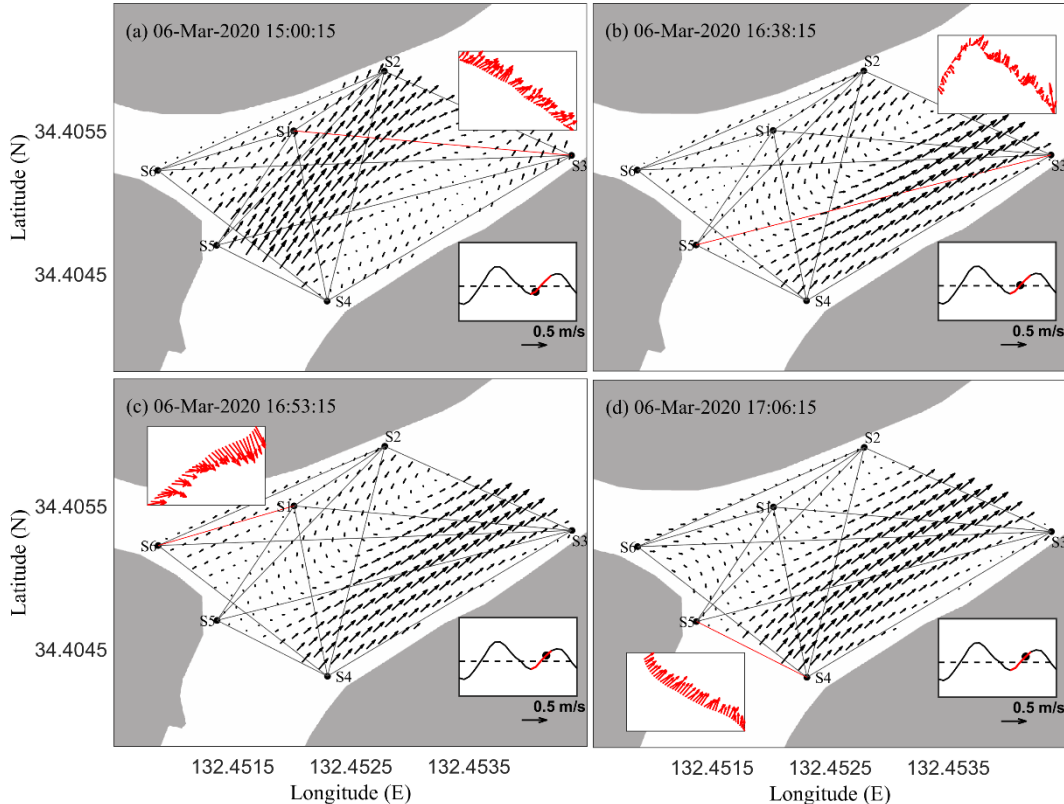


Figure 6. Relationships between FAT and ADCP are shown (a) eastward and (b) northward velocity components. The coefficient of determination (R^2) and the root mean square error (RMSE) are given at the right side of each panel.

Moreover, Figure 7 compares the depth-averaged velocity directions obtained

275 from moving-boat ADCP measurements against those derived from FAT. Despite the
 276 fundamental and essential differences between these two techniques, the behaviors of
 277 tidal velocity shown in Figure 7 indicate that there is a well agreement between these
 278 two different techniques at the tidal junction.



279
 280 Figure 7. Typical Depth-averaged current structures from FAT during the StreamPro
 281 ADCP observation period. The red solid lines connecting the acoustic stations
 282 represent the StreamPro ADCP observation routes. The velocity directions along the
 283 ADCP routes are shown in the sub-figure of each panel. The tidal phase of each
 284 sub-figure is signaled by a black dot on the water level at the lower right corner.

285 3.3 Tidal distortion and asymmetry at the junction

286 In estuarine systems, due to the interactions of tidal harmonics, the tidal response
 287 is generally described by the progress of tidal distortion and asymmetry. The M_2 and M_4
 288 tides are the most crucial astronomical and shallow-water components, respectively.
 289 Hence, Friedrichs and Aubrey (1988) proposed a mathematical relationship between
 290 M_2 and M_4 , which is utilized as the indicators of tidal distortion and asymmetry. The
 291 inverse method calculates the depth-averaged velocity at each computational grid point.
 292 Thus, the inversed velocity results with 1-min intervals were directly applied to a
 293 point-by-point classical tidal harmonic analysis to acquire the M_2 and M_4 tidal
 294 constituents (Pawlowicz et al., 2002).

295 Figure 8 shows the spatial distributions of these two indicators at the junction. The
 296 distorted tide had an M_4/M_2 amplitude ratio greater than zero (Figure 8a); the larger the

values of the M_4/M_2 amplitude ratio, the more significant the tidal distortion. The mean flood and ebb durations at Missasa gauging station were around 5.5 h and 6.9 h, respectively, with a 1.4 h difference in tidal durations. The velocity phase of $2M_2-M_4$ showed both types of asymmetric distortion at the junction (Figure 8b). From the Tenma River region to line S1-S5, the velocity phase indicator indicated an ebb-dominant asymmetric distortion. The type becomes a flood asymmetry in the Kyu Ota River region. As presented in Table 1, the results of the velocity data of three fixed ADCP stations confirmed the same type of asymmetric distortion at the three positions. Flood-dominated systems usually refer to the asymmetry characteristics of the flood duration is shorter than the ebb duration in tidal water levels and the higher flood velocity during flood tide larger than that during the ebb tide (Friedrichs & Aubrey, 1988). In ebb-dominated systems, the relationship is reversed.

The two indicators reflect the combined effects of tidal energy transfer and frictional dissipation at the junction. The ebb dominance type in the Tenma River region is mainly a result of extensive tidal flats. The tidal flats cause higher bed levels in the Tenma River region than in the Kyu Ota River region and lead a slower rate of non-linear growth of M_2 (Friedrichs & Aubrey, 1988).

Table 1. Amplitude and phase of M_2 and M_4 of the velocity data of the three fixed ADCP stations obtained by harmonic analysis.

	M_2		M_4		M_4/M_2	$2M_2-M_4$ (°)
	Amplitude (m/s)	Phase (°)	Amplitude (m/s)	Phase (°)		
S1-ADCP	0.0795	35.63	0.0162	284.93	0.21	-213.67
S3-ADCP	0.1003	33.53	0.0318	281.66	0.32	-214.60
S5-ADCP	0.1135	60.57	0.0115	85.28	0.11	35.86

The tidal harmonic length analyses at S1-ADCP, S3-ADCP, and S5-ADCP were performed from February 21 to March 9, February 21 to March 13, and February 21 to March 7, respectively.

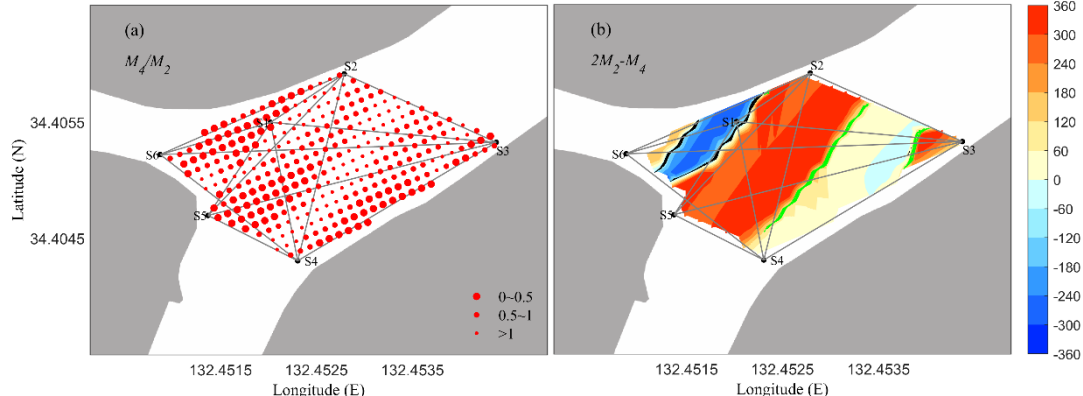


Figure 8. Distributions of (a) the M_4/M_2 ratio of the velocity amplitudes, and (b) the $2M_2-M_4$ of velocity phase in degrees. The green (black) lines in (b) represent the 90°

324 (-90°) contour lines.

325 4. Discussion

326 4.1 Evaluation of the inversion results

327 The spatial resolution ΔR ($\Delta R = \sqrt{\frac{A}{N}}$) is decided by the number of acoustic
 328 transmission rays within the tomography area (Park & Kaneko, 2001). A represents the
 329 tomography area (~52700 m²), and N is the amount of successfully transmitted rays (N
 330 <= 14). The highest spatial resolution of the acoustic array was around 7.8 m in this
 331 work.

332 During the damped least-squares method, the damping factor α was used to
 333 stabilize the inverse analysis solutions (Yamaguchi et al., 2005; Yamoaka et al., 2002).
 334 For the damped least-squares method, the expected error covariance matrix U
 335 (uncertainty) of the solutions can be written as

$$336 U = I - E^T(EE^T + \alpha^2 I)^{-1}E \quad (2)$$

337 By multiplying the vector P comprised the harmonic functions emerging in the
 338 Fourier series, matrix U is converted into S in a physical area:

$$339 S = P^T UP \quad (3)$$

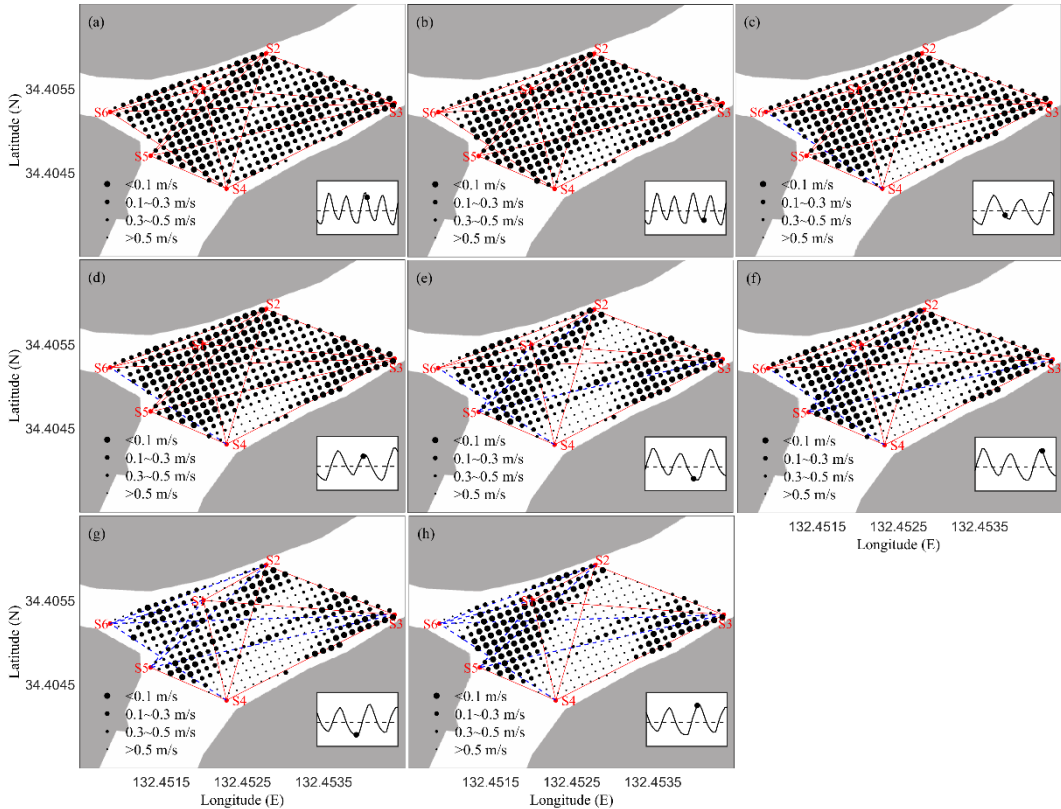
340 The diagonal elements of S represent the uncertainties of the inverse analysis
 341 solutions in the tomography domain. The amount and layout of successfully
 342 transmitted rays and the values of the damping factor α calculated by the L curve
 343 method mainly regulate the uncertainties.

344 Regarding the specificity of the study area, the reciprocal sound transmissions
 345 related to S5 and S6 are important to obtain the inverse results. Here, we conducted
 346 several cases to discuss the uncertainties of the inverse results.

347 Case I (N=14): In most of the inverse area, the uncertainties were less than 0.1 m/s
 348 in the tomography domain (Figure 9a, 9b). Higher uncertainties were always exhibited
 349 around S4 and at the center of the tomography domain (Figure 9a, 9b). Case II (lack of
 350 S4-S6): similar to Case I, most of the values were less than 0.1 m/s (Figure 9c, 9d).
 351 Case III (lack of S4-S6, S1-S5, S2-S5, and S3-S5) and Case IV (lack of S4-S6, S1-S5,
 352 S2-S5, S3-S5, S1-S6, S2-S6, and S3-S6) showed a significant increase in uncertainties.
 353 Specifically, the uncertainties showed a dramatic increase when the case changed from
 354 Case III to Case IV. The spatially averaged uncertainties of a (Case I, high water), b
 355 (Case I, low water), c (Case II, low water), d (Case II, high water), e (Case III, low
 356 water), f (Case III, high water), g (Case IV, low water), and h (Case IV, high water),
 357 followed the proportions of 1.0: 1.1: 1.29: 1.22: 2.23: 1.91: 3.23: 3.98.

358 Under ideal conditions, observations with more FAT stations and higher
 359 frequencies will acquire more precise results at the shallow tidal junction. Zhang et al.
 360 (2017) conducted an experiment with 11 coastal acoustic tomography (CAT) systems
 361 in Dalian Bay to discuss the tidal current structures. The precision of their observations

362 was the highest thus far because of the largest number of transmission rays (51) that
 363 ever recorded in the previous studies, but the observation period was limited to one day.
 364 The related data in Section 3.2 show satisfactory results for the current distribution.
 365 However, the successful acquisition rates of the 14 sound transmission rays had a wide
 366 variation (19%–92%, Figure 2b). Overall, this study scheme performed well
 367 (considering observation period and precision) adjacent to the tidal junction.



368

369

Figure 9. Uncertainty maps for inverse solutions of some typical cases.

370

4.2 Dynamic mechanisms of tidal currents at the junction

371

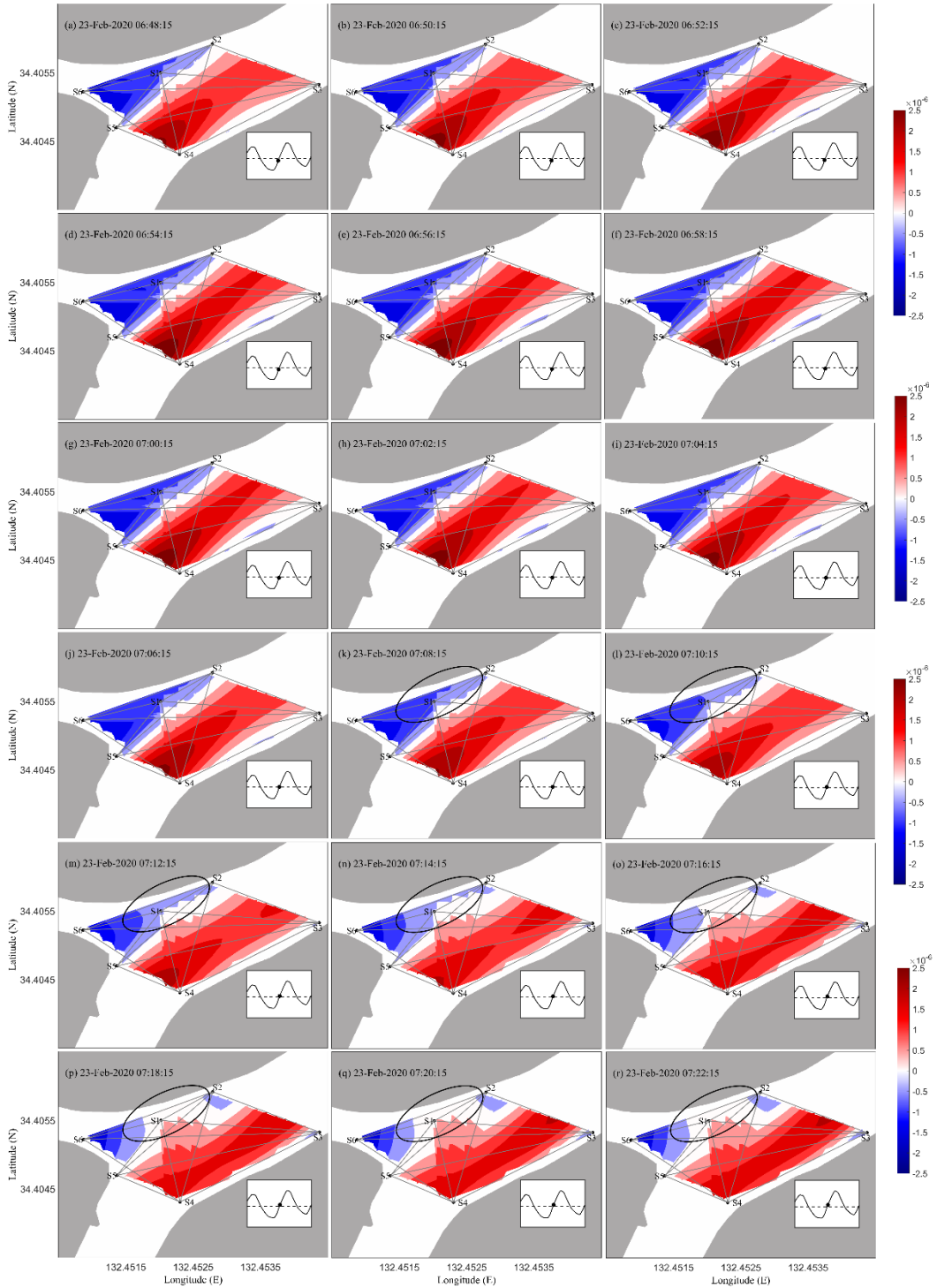
372

373

374

375

As shown in Section 3.2.1 (Figure 5), the transformation of flow patterns took place during the flood tide in the area around the confluence location (S5). To understand the processes of flow pattern formation, we calculated the relative vorticity ($\zeta = \frac{\partial v}{\partial x} - \frac{\partial u}{\partial y}$, u and v represent the eastward and northward velocity components inversed by FAT, respectively) during the flood tide at the junction.



376

377 Figure 10. Maps of the relative vorticity during the flood tide corresponding to the
 378 horizontal current distributions in Figure 5.

379

380 As shown in Figure 10, positive and negative ζ appeared in the Kyu Ota River
 381 and Tenma River regions, respectively. This results from the geometry of the junction.
 382 The tide in the Tenma River region is dominated by a west-eastward direction, while it
 383 is dominated by a northeast-southwestward direction in the Kyu Ota River region. The

384 flow patterns exhibited transformations of the current (Figure 5k to Figure 5p) and
 385 vorticity patterns (Figure 10k to Figure 10p). The area with negative ζ values (blue)
 386 gradually decreased, while the area with positive ζ values (red) gradually extended to
 387 lines S1-S2 (Figure 10k-10p). Danial et al. (2019) indicated that the Tenma River is
 388 more convergent than the Kyu Ota River, resulting in a larger phase difference in the
 389 tidal discharge/tidal velocity at the Tenma River. Additionally, Danial et al. (2019)
 390 revealed that the tidal discharge phase at the Tenma River was ahead by ~15-min as
 391 compared with that at the Kyu Ota River. The tidal discharges were well related to the
 392 tidal velocities. The nonlinear effect leads to some differences when the tidal wave
 393 propagates from the river mouth to the junction through these two different branches
 394 during the flood tide. The phase difference (φ) and phase lag (ε) have a relationship
 395 with $\varepsilon + \varphi = \frac{\pi}{2}$. Thus, it can be inferred that the transformation of the tidal current
 396 patterns during flood tide results from the phase difference/phase lag. The quick
 397 processes of decay and transformation of tidal current patterns are a difficult target for
 398 the fixed ADCP or moving-boat ADCP; however, the FAT observations allow us to
 399 investigate such patterns. This study further demonstrates the fascinating application
 400 (continuous measurement of 2D flow pattern) of FAT in shallow water environments.

401 The flow directions in the survey area can be explained by the geometry of the
 402 junction. The geometry of the junction results in a large curvature in the flow directions
 403 when the flow enters the tomography domain. Overall, as shown in section 3.2,
 404 streamlines tend to follow the shape of the riverbanks.

405 **4.3 Tidal propagation and damping at the junction**

406 Based on the harmonic analysis of the water level (Table 2), we selected 13
 407 significant tidal constituents to discuss the propagation and dampening process of the
 408 tide at the junction. The inversed velocity data with 1-min intervals were applied to a
 409 point-by-point classical tidal harmonic analysis to acquire the 13 tidal constituents. The
 410 spatial variabilities of the 13 tides are presented in Figure 11. The spatially averaged
 411 tidal current amplitudes of Mm , MSf , K_1 , O_1 , Q_1 , M_2 , S_2 , N_2 , L_2 , M_4 , MS_4 , M_6 , and M_8 ,
 412 followed the proportions of 1.00: 0.72: 0.62: 0.48: 0.33: 2.78: 1.42: 0.66: 0.84: 0.25:
 413 0.60: 0.25: 0.20.

414

415 Table 2. Amplitude and phase of 13 significant tidal components at Eba and Misasa
 416 gauging stations obtained by tidal harmonic analysis of 35 days of water level data.

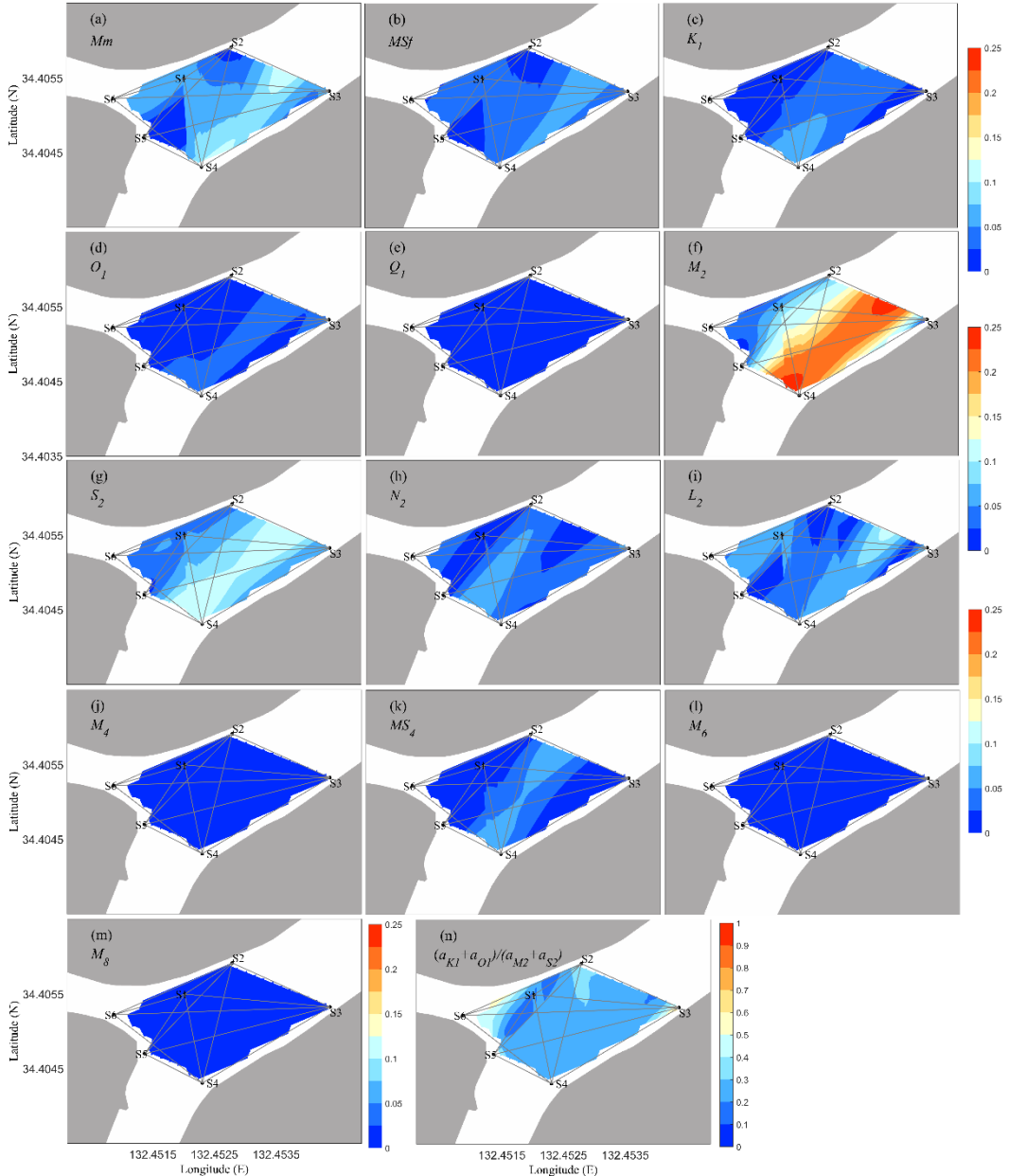
	Eba	Misasa		
Tidal Constituent	Amplitude (m)	Phase (°)	Amplitude (m)	Phase (°)
Mm	0.0569	12.77	0.1417	22.29
MSf	0.0180	308.71	0.0932	0.0932
K_1	0.2269	233.53	0.1855	231.69
O_1	0.2225	186.33	0.1770	183.72

Q_1	0.0532	166.03	0.0336	173.36
M_2	0.9867	274.33	0.8560	279.10
S_2	0.5274	324.92	0.4275	326.98
N_2	0.2077	265.39	0.1529	274.26
L_2	0.0833	294.64	0.1466	299.23
M_4	0.0170	43.60	0.0712	165.05
MS_4	0.0248	97.28	0.0634	213.82
M_6	0.0225	136.87	0.0149	230.16
M_8	0.0001	242.52	0.0100	92.99

417

418 As shown in Figure 11, low-frequency tides became stronger at the tidal junction.
 419 The monthly tide (M_m , $T \approx 27.6$ d) and the fortnightly tide (MS_f , $T \approx 14.8$ d) were more
 420 significant than diurnal tides. Godin (1999) showed that in a tidal river, most linear
 421 tidal components will be damped more quickly than M_2 , while some tidal constituents
 422 might be enhanced by nonlinear energy transfer or resonance. The M_6 and M_8 tide
 423 constituents were insignificant compared to other shallow-water constituents and
 424 remained constant at the junction (Figures 11l and 11m). The variations in the tidal
 425 currents at the junction were dominated by semidiurnal species (D2: M_2 , S_2 , N_2 , L_2),
 426 followed by diurnal species (D1: K_1 , O_1 , Q_1) and quarter-diurnal species (D4: M_4 , MS_4).
 427 This indicates that at the junction, the shallow water effect does not trigger the tidal
 428 distortion of D2 well; thus, it cannot generate sufficient energy to convert D2 to D4.
 429 Here, the surveyed tidal channel junction is situated only 5.8 km upstream from the
 430 estuary, implying that the tide should propagate more to upriver areas to generate D4.

431 Tidal characteristics can be recognized using the form number (Pugh, 1987), and
 432 it is determined by the amplitude ratio between the main diurnal and semidiurnal tidal
 433 constituents ($F = (a_{K1} + a_{O1}) / (a_{M2} + a_{S2})$). The form number of the water level at the Eba
 434 and Misasa gauging station was 0.29 and 0.28, indicating that the tide is of a mixed
 435 type. The form numbers of tidal velocity varied at the junction (Figure 11n), mostly
 436 between 0.25 and 1, with higher values in the Kyu Ota River. The form number
 437 indicated that the tidal regime at the junction can be deemed to be of a mixed type.



438

439 Figure 11. (a)–(m) distributions of the amplitude of the 13 tidal components (M_m , MS_f ,
 440 K_1 , O_1 , Q_1 , M_2 , S_2 , N_2 , L_2 , M_4 , MS_4 , M_6 , and M_8) at the junction; (n)
 441 amplitude ratio $((a_{K1} + a_{O1})/(a_{M2} + a_{S2}))$ between the main diurnal and semidiurnal tidal constituents.
 442

443 Nontidal forcing (e.g., river discharge) contributes to sub-tide species, affecting
 444 tidal lists to remove these tide constituents as contaminated by noise (Ray & Erofeeva,
 445 2014). For example, In the Yangtze River Estuary, Guo et al. (2015) reported that river
 446 discharge can strongly induce substantial annual mean water level differences and
 447 related differences in tidal amplitudes; however, river discharge restricted variations in
 448 the monthly and fortnightly tidal frequencies. In other words, interactions between tidal
 449 components are an important reason for tidal low-frequency variations in tide
 450 propagating processes and generated low-frequency tides. The interaction of M_2 and S_2

451 caused fortnightly (MSf) variations in tidal properties ($\omega_{M2}-\omega_{S2}=\omega_{MSf}$, ω is tidal
 452 frequency); the interaction of M_2 and N_2 caused monthly (Mm) tidal variations
 453 ($\omega_{M2}-\omega_{N2}=\omega_{Mm}$). The production of such compound tides suggests a tidal energy
 454 transfer from semidiurnal frequencies to sub-tide frequencies (Gallo & Vinzon, 2005).
 455 Similar interactions also exist between other semidiurnal and diurnal tides. Usually, the
 456 tidal potential includes limited energy at the MSf and Mm tidal frequencies, and
 457 becomes negligible in the upstream areas of a river (Zhang et al., 2012). But, as shown
 458 in Figures 11a and 11b, the MSf and Mm tides grew strongly. During low-flow days, the
 459 freshwater discharge in the upriver only varies between 20 and 50 m³/s (Danial et al.,
 460 2019). The role of freshwater discharge at the junction is negligible during low-flow
 461 periods. Thus, fortnightly and monthly subtidal variations at the junction are mainly
 462 controlled by the tidal interactions; they are also mediated by river flow but not directly
 463 at the junction.

464 While the tides propagate along the channel, the tidal dampening process is
 465 dramatically affected by the friction effect, followed a decreased tidal range in space.
 466 In this study, owing to the lack of temporal-spatial distributions of tidal ranges along
 467 the channel, we only compared the tidal range between two gauging stations (Eba,
 468 Misasa). As shown in Figure 12b, fortnightly variations in tidal ranges were evident at
 469 both the Eba and Misasa stations, and a decreasing trend of the tidal ranges was
 470 manifested along the channel. In convergent estuaries, the enhancement and
 471 attenuation of tidal energy are considerably governed by the relative intensity of
 472 dissipation versus local inertia in the momentum equation, also the function of channel
 473 convergence in the mass balance (van Rijn, 2011). On the other hand, strongly
 474 convergent shallow estuaries was investigated by Friedrichs and Aubrey (1994), the
 475 findings indicated that they are dynamically controlled by friction and kinematically
 476 influenced by convergence. As the channel convergence increases, the characteristics
 477 of tidal distortion are increased, alternatively speed and wavelength of tidal wave
 478 significantly decrease (Lu et al., 2015). In the case of weakly dissipative estuaries, tide
 479 propagation feature can be described by a feebly nonlinear behavior, and over-tides are
 480 produced in a cascade process, so that the higher harmonics have progressively reduced
 481 amplitudes (Lanzoni & Seminara, 1998). For this study, although the shallow water
 482 depth and convergent width might increase the tides to some degree, the declining
 483 trend during the spring tide suggests that the tidal channel is a strongly dissipative
 484 channel accompanied by strong nonlinear effects.

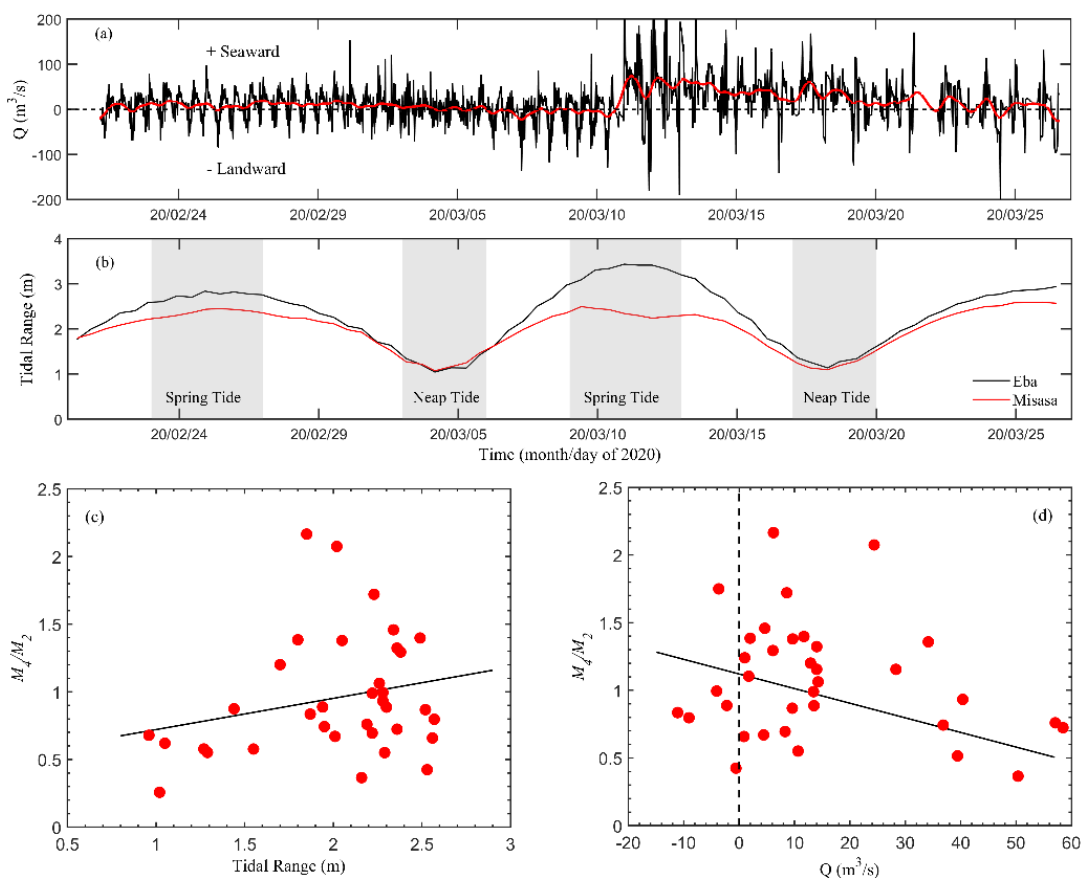
485 4.4 River-Tide interactions at the junction

486 River flow significantly influences tidal dynamics by decreasing the tidal
 487 amplitudes, obstructing wave propagation, and modifying the tidal energy distribution
 488 between tidal frequencies (Sassi & Hoitink, 2013). Theoretical analysis suggests that a
 489 tidal channel with constant depth and width causes a roughly linear relationship
 490 between tidal damping coefficients and streamflow, and the amplitude of the incident
 491 wave from the estuary to the upstream areas varies with the square root of river flow

492 (Jay & Flinchem, 1997). However, the tidal damping process is nonlocal. Therefore,
 493 the independent impacts on tidal damping induced by a varying river flow are not easy
 494 to quantify (Kukulka & Jay, 2003).

495 River flow also modifies the interactions between tidal constituents and the
 496 subsequent generation of over-tides and compound tides. This process is clearly
 497 revealed by the reduced M_4 amplitude during high flow periods, whereas the amplitude
 498 ratio of the M_4/M_2 was larger during low flow periods (Figure 12d). This reflects the
 499 more significant tidal wave deformation that occurred during the high flow periods.
 500 River flow plays a crucial role in river flow enhanced subtidal friction, which
 501 significantly diminishes the tidal energy at the upstream whilst triggering tidal energy
 502 transfer from the primary tides to over-tides at the downstream (Cai et al., 2014).

503 Additionally, river-tidal interactions significantly disturb the characteristic of tidal
 504 asymmetry. Some studies observed a landward increase in the amplitude of the M_4/M_2
 505 ratio with a damping of the M_2 tide and noted a significant decline in the amplitude of
 506 the M_4/M_2 ratio from spring to neap tide (Guo et al., 2015; Lu et al., 2015). In this work,
 507 we also found larger M_4/M_2 amplitude ratios during spring than that during neap tide
 508 (Figure 12c), indicating that the M_2 tide progressively transformed to the M_4 tide from
 509 neap tide to spring tide.



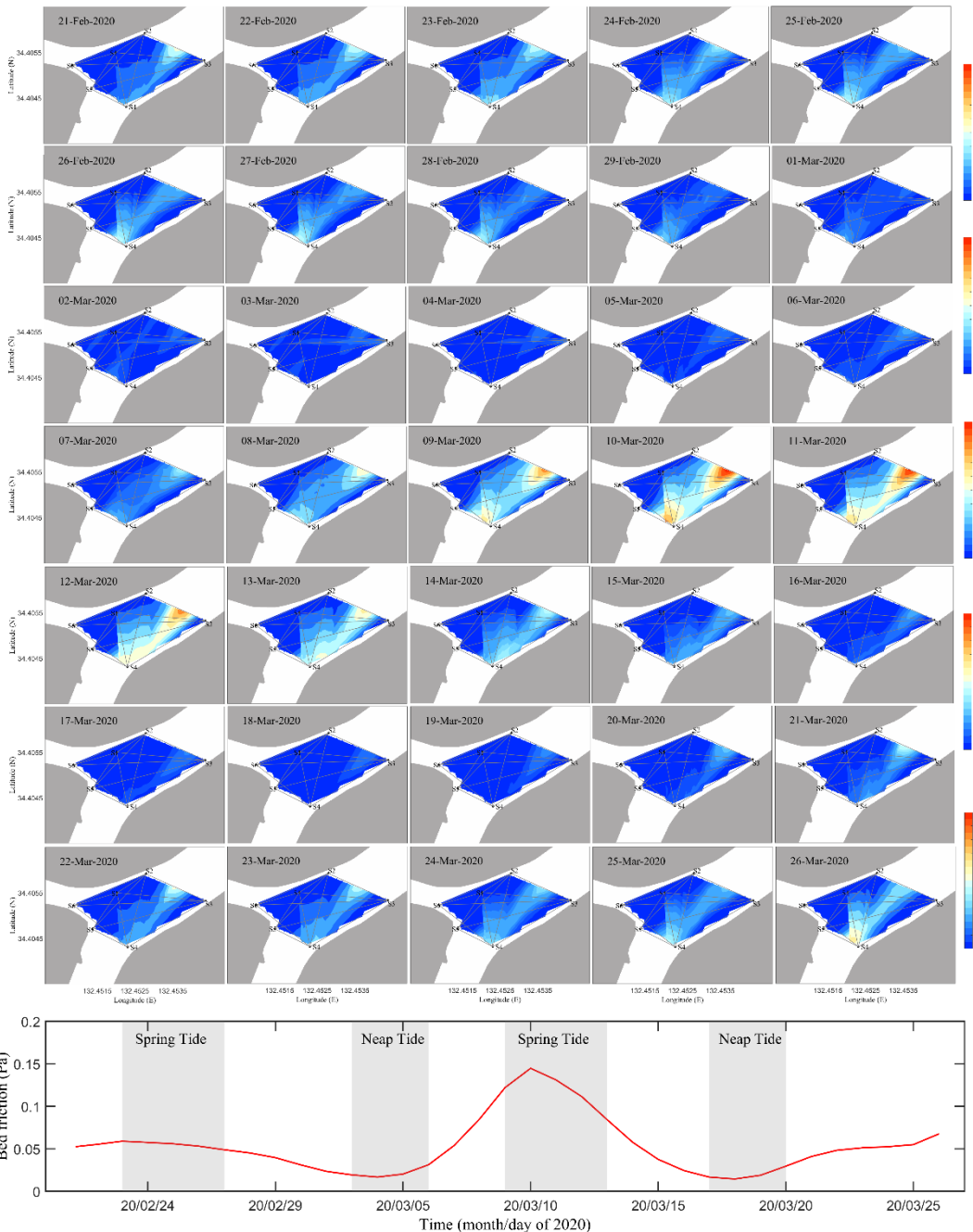
510
 511 Figure 12. (a) tidal discharge in the Kyu Ota River; the tidal discharge was calculated
 512 from the transmission line S2-S3 (Figure 1b); (b) tidal ranges at two water level
 513 gauging stations (Eba and Misasa); (c) relationship between the daily spatially

514 averaged amplitude of the M_4/M_2 ratio and daily tidal range; and (d) relationship
515 between the daily spatially averaged amplitude of the M_4/M_2 ratio and daily river
516 discharge.

517

518 The nonlinear tide M_4 and its related tidal asymmetry are one of the most
519 important mechanisms causing residual suspended sediment transport in estuarine
520 environments (Hoitink & Jay, 2016). For this study, at the tidal junction of the Ota
521 River estuarine system, river flow is limited during the normal situation, so that the
522 influences resulting from tide-induced asymmetric currents are noteworthy for
523 suspended sediment transport (Xiao et al., 2020). This is different from the situation in
524 the Yangtze River estuary because of river discharge is so strong (6000–92000 m³/s)
525 that the enhanced ebb-directed sediment transport by the river flow is significant, while
526 the roles of tide-induced asymmetric currents are negligible in suspended sediment
527 transport mechanisms (Guo et al., 2014). The interactions between river and tide and
528 the resultant tidal asymmetry are crucial at the junction or at the Ota River estuary.
529 They may cause significant variations in water levels and bed frictions, which have
530 continuous effects on the process of erosion, deposition, and transport of sediment.
531 Here, we estimated the bed friction from tidal currents, following the basic equations
532 shown in Cea and Vázquez-Cendón (2012). Temporally, a higher bed friction occurred
533 during the spring periods than during the neap periods. Spatially, bed friction at the
534 junction showed that values in the Kyu Ota River were higher than those in the Tenma
535 River (Figure 13). The bathymetry distribution revealed that the eastern channel region
536 is deeper than the western channel region at the junction, which demonstrates the role
537 of bed friction. Bed friction plays a fundamental role in sediment motion and
538 moderately modifies the basin geometry and bathymetry.

539



540

541 Figure 13. Daily bed friction (Pa) distribution estimated from tidal currents and
 542 variations in the daily spatially averaged bed friction from 21 February to 26 March,
 543 2020.

544 5. Conclusions

545 For the first time, continuous 2D tidal current fields were measured at a shallow
 546 junction using fluvial acoustic tomography (FAT) systems composed of six fixed
 547 acoustic stations from February 21 to March 26, 2020. The horizontal structure and the
 548 spatiotemporal variation of the tidal velocities were well revealed by FAT. In total,

549 actual reciprocal sound transmissions were performed during ~ 34.4 days along 14
550 transmission lines. The horizontal tidal velocities estimated by inverse analysis agreed
551 well with the fixed ADCP and the moving-boat ADCP velocities.

552 Temporally, tidal currents during ebb tide were higher than during flood tide.
553 Spatially, tidal currents in the Kyu Ota River region were stronger than those in the
554 Tenma River region. Tidal currents tended to be slow and separated into two parts in
555 the area around the confluence location. The high frequency observation interval
556 (1-min) used in this study provided an effective way to detect the rapid processes of the
557 transformation of tidal current patterns during flood tide at the junction. These results
558 demonstrate that FAT is a fascinating tool for continuously mapping variable 2D tidal
559 current structures at shallow tidal junctions. Furthermore, several case studies were
560 performed to appraise the influence of the acoustical ray number and bathymetry on the
561 inverse results. Overall, this work showed a good performance of the employed
562 methods (observation period and precision) at the tidal junction. The velocity
563 amplitude ratio of M_4/M_2 showed that the tidal distortion was significant at the junction,
564 and the velocity phase of $2M_2-M_4$ indicated both two types of asymmetric distortions at
565 the junction.

566 The tidal harmonic analysis method was adopted for the tidal currents
567 reconstructed by the inversion of the FAT data. Further, the comprehensive evolution
568 processes of tidal asymmetry, tidal distortion, tidal dampening, and tidal propagation at
569 the junction were studied and discussed. The spatial distributions of 13 tidal
570 constituents allowed to clearly disentangle the evolution process of sub-tide species
571 (M_m , MS_f), semidiurnal species (D2: M_2 , S_2 , N_2 , L_2), diurnal species (D1: K_1 , O_1 , Q_1),
572 and quarter-diurnal species (D4: M_4 , MS_4). The ratios of the tidal current amplitudes of
573 M_m , MS_f , K_1 , O_1 , Q_1 , M_2 , S_2 , N_2 , L_2 , M_4 , MS_4 , M_6 , and M_8 were 1.00: 0.72: 0.62: 0.48:
574 0.33: 2.78: 1.42: 0.66: 0.84: 0.25: 0.60: 0.25: 0.20, respectively.

575 This study demonstrated that the application of FAT in conjunction with the
576 inverse method presents an effective tool to map 2D tidal currents and to investigate the
577 propagation and damping of tidal currents in a shallow tidal junction in detail.

578 Acknowledgments

579 Cong Xiao is very thankful for the China Scholarship Council (CSC) in
580 supporting his doctoral course at Hiroshima University. This work was financed by the
581 Japan Society for the Promotion of Science (JSPS) KAKENHI grant number
582 JP17H03313. We acknowledge the students who joined us during the field work for
583 their assistance with data collection. We would like to thank Dr. Chuanzheng Zhang
584 (State Key Laboratory of Satellite Ocean Environment Dynamics, Second Institute of
585 Oceanography, State Oceanic Administration, China), and Dr. Minmo Chen and
586 Professor Arata Kaneko of Hiroshima University for their valuable suggestions for
587 analyzing the data. Also, we are thankful for Editage (www.editage.com) for its
588 assistant given for the English language.

589 The water level data at Misasa and Eba gauging stations were download from the
 590 Ministry of Land, Infrastructure, Transport and Tourism (<http://www1.river.go.jp>), and
 591 precipitation data were downloaded from the Japan Meteorological Agency
 592 (<http://www.jma.go.jp>). The data used in this study for reproducing the figures are
 593 available by contacting Kiyosi Kawanisi, Hiroshima University
 594 (kiyosi@hiroshima-u.ac.jp).
 595

596 References

- 597 Cai, H., Savenije, H., & Toffolon, M. (2014). Linking the river to the estuary:
 598 influence of river discharge on tidal damping. *Hydrology and Earth System Sciences*,
 599 18(1), 287.
- 600 Cai, H., Yang, Q., Zhang, Z., Guo, X., Liu, F., & Ou, S. (2018). Impact of river-tide
 601 dynamics on the temporal-spatial distribution of residual water level in the Pearl
 602 River channel networks. *Estuaries and Coasts*, 41(7), 1885-1903.
- 603 Cea, L., & Vázquez-Cendón, M. E. (2012). Unstructured finite volume discretisation
 604 of bed friction and convective flux in solute transport models linked to the shallow
 605 water equations. *Journal of Computational Physics*, 231(8), 3317-3339.
- 606 Danial, M. M., Kawanisi, K., & Al Sawaf, M. B. (2019). Characteristics of tidal
 607 discharge and phase difference at a tidal channel junction investigated using the
 608 fluvial acoustic tomography system. *Water*, 11(4), 857.
- 609 Dinehart, R., & Burau, J. (2005). Repeated surveys by acoustic Doppler current
 610 profiler for flow and sediment dynamics in a tidal river. *Journal of Hydrology*,
 611 314(1-4), 1-21.
- 612 Friedrichs, C. T., & Aubrey, D. G. (1988). Non-linear tidal distortion in shallow
 613 well-mixed estuaries: a synthesis. *Estuarine, Coastal and Shelf Science*, 27(5),
 614 521-545.
- 615 Friedrichs, C. T., & Aubrey, D. G. (1994). Tidal propagation in strongly convergent
 616 channels. *Journal of Geophysical Research: Oceans*, 99(C2), 3321-3336.
- 617 Gallo, M. N., & Vinzon, S. B. (2005). Generation of overtides and compound tides in
 618 Amazon estuary. *Ocean Dynamics*, 55(5-6), 441-448.
- 619 Godin, G. (1999). The propagation of tides up rivers with special considerations on
 620 the upper Saint Lawrence River. *Estuarine, Coastal and Shelf Science*, 48(3),
 621 307-324.
- 622 Guo, L., Van der Wegen, M., Roelvink, J., & He, Q. (2014). The role of river flow
 623 and tidal asymmetry on 1-D estuarine morphodynamics. *Journal of Geophysical
 624 Research: Earth Surface*, 119(11), 2315-2334.
- 625 Guo, L., van der Wegen, M., Jay, D. A., Matte, P., Wang, Z. B., Roelvink, D., et al.
 626 (2015). River-tide dynamics: Exploration of nonstationary and nonlinear tidal
 627 behavior in the Y angtze R iver estuary. *Journal of Geophysical Research: Oceans*,
 628 120(5), 3499-3521.

- 629 Hoitink, A., & Jay, D. A. (2016). Tidal river dynamics: Implications for deltas.
630 *Reviews of Geophysics*, 54(1), 240-272.
- 631 Jay, D. A., & Flinchem, E. P. (1997). Interaction of fluctuating river flow with a
632 barotropic tide: A demonstration of wavelet tidal analysis methods. *Journal of*
633 *Geophysical Research: Oceans*, 102(C3), 5705-5720.
- 634 Kaneko, A., Yuan, G., Gohda, N., & Nakano, I. (1994). Optimum design of the ocean
635 acoustic tomography system for the Sea of Japan. *Journal of Oceanography*, 50(3),
636 281-293.
- 637 Kawanisi, K., Razaz, M., Kaneko, A., & Watanabe, S. (2010). Long-term
638 measurement of stream flow and salinity in a tidal river by the use of the fluvial
639 acoustic tomography system. *Journal of Hydrology*, 380(1-2), 74-81.
- 640 Kawanisi, K., Razaz, M., Yano, J., & Ishikawa, K. (2013). Continuous monitoring of
641 a dam flush in a shallow river using two crossing ultrasonic transmission lines.
642 *Measurement Science and Technology*, 24(5), 055303.
- 643 Kukulka, T., & Jay, D. A. (2003). Impacts of Columbia River discharge on salmonid
644 habitat: 1. A nonstationary fluvial tide model. *Journal of Geophysical Research:*
645 *Oceans*, 108(C9).
- 646 Lanzoni, S., & Seminara, G. (1998). On tide propagation in convergent estuaries.
647 *Journal of Geophysical Research: Oceans*, 103(C13), 30793-30812.
- 648 Lu, S., Tong, C., Lee, D. Y., Zheng, J., Shen, J., Zhang, W., et al. (2015). Propagation
649 of tidal waves up in Yangtze Estuary during the dry season. *Journal of Geophysical*
650 *Research: Oceans*, 120(9), 6445-6473.
- 651 Munk, W., Worcester, P., & Wunsch, C. (1995). Ocean acoustic tomography,
652 Cambridge Univ. Pr, Cambridge UK.
- 653 Park, J.-H., & Kaneko, A. (2001). Computer simulation of coastal acoustic
654 tomography by a two-dimensional vortex model. *Journal of Oceanography*, 57(5),
655 593-602.
- 656 Pawlowicz, R., Beardsley, B., & Lentz, S. (2002). Classical tidal harmonic analysis
657 including error estimates in MATLAB using T_TIDE. *Computers & Geosciences*,
658 28(8), 929-937.
- 659 Pugh, D. T. (1987). Tides, surges and mean sea level.
- 660 Ray, R. D., & Erofeeva, S. Y. (2014). Long-period tidal variations in the length of day.
661 *Journal of Geophysical Research: Solid Earth*, 119(2), 1498-1509.
- 662 Razaz, M., Kawanisi, K., Nistor, I., & Sharifi, S. (2013). An acoustic travel time
663 method for continuous velocity monitoring in shallow tidal streams. *Water Resources*
664 *Research*, 49(8), 4885-4899.
- 665 Razaz, M., Kawanisi, K., Kaneko, A., & Nistor, I. (2015). Application of acoustic
666 tomography to reconstruct the horizontal flow velocity field in a shallow river. *Water*
667 *Resources Research*, 51(12), 9665-9678.
- 668 Razaz, M., Kawanisi, K., Nistor, I., & Zedel, L. (2016). Depth-Averaged Flow
669 Reconstruction in an Extremely Shallow Estuary. Ottawa, Canada, May 10-13,
670 2016.

- 671 Sassi, M., Hoitink, A., de Brye, B., & Deleersnijder, E. (2012). Downstream
672 hydraulic geometry of a tidally influenced river delta. *Journal of Geophysical
673 Research: Earth Surface*, 117(F4).
- 674 Sassi, M., & Hoitink, A. (2013). River flow controls on tides and tide-mean water
675 level profiles in a tidal freshwater river. *Journal of Geophysical Research: Oceans*,
676 118(9), 4139-4151.
- 677 van Rijn, L. C. (2011). Analytical and numerical analysis of tides and salinities in
678 estuaries; part I: tidal wave propagation in convergent estuaries. *Ocean Dynamics*,
679 61(11), 1719-1741.
- 680 Xiao, C., Kawanisi, K., & Al Sawaf, M. B. (2020). Suspended particulate matter
681 concentration in response to tidal hydrodynamics in a long mesotidal floodway.
682 *Estuarine, Coastal and Shelf Science*, 233, 106525.
- 683 Yamaguchi, K., Lin, J., Kaneko, A., Yayamoto, T., Gohda, N., Nguyen, H.-Q., et al.
684 (2005). A continuous mapping of tidal current structures in the Kanmon Strait.
685 *Journal of Oceanography*, 61(2), 283-294.
- 686 Yamoaka, H., Kaneko, A., Park, J.-H., Zheng, H., Gohda, N., Takano, T., et al. (2002).
687 Coastal acoustic tomography system and its field application. *IEEE Journal of
688 Oceanic Engineering*, 27(2), 283-295.
- 689 Zhang, C., Zhu, X.-H., Zhu, Z.-N., Liu, W., Zhang, Z., Fan, X., et al. (2017).
690 High-precision measurement of tidal current structures using coastal acoustic
691 tomography. *Estuarine, Coastal and Shelf Science*, 193, 12-24.
- 692 Zhang, E., Savenije, H., Chen, S., & Mao, X. (2012). An analytical solution for tidal
693 propagation in the Yangtze Estuary, China. *Hydrology & Earth System Sciences*,
694 16(9).
- 695 Zhu, X.-H., Zhu, Z.-N., Guo, X., Ma, Y.-L., Fan, X., Dong, M., et al. (2015).
696 Measurement of tidal and residual currents and volume transport through the
697 Qiongzhou Strait using coastal acoustic tomography. *Continental Shelf Research*, 108,
698 65-75.
- 699